Lab on a Chip

Accepted Manuscript

This is an *Accepted Manuscript*, which has been through the Royal Society of Chemistry peer review process and has been accepted for publication.

Accepted Manuscripts are published online shortly after acceptance, before technical editing, formatting and proof reading. Using this free service, authors can make their results available to the community, in citable form, before we publish the edited article. We will replace this *Accepted Manuscript* with the edited and formatted *Advance Article* as soon as it is available.

You can find more information about *Accepted Manuscripts* in the Information for Authors.

Please note that technical editing may introduce minor changes to the text and/or graphics, which may alter content. The journal's standard Terms & Conditions and the Ethical guidelines still apply. In no event shall the Royal Society of Chemistry be held responsible for any errors or omissions in this *Accepted Manuscript* or any consequences arising from the use of any information it contains.

ROYAL SOCIETY OF CHEMISTRY

www.rsc.org/loc

Caterpillar Locomotion–inspired Valveless Pneumatic Micropump using Single Teardrop-shaped Elastomeric Membrane

Hongyun So[a], Albert P. Pisano[a], and Young Ho Seo[b,*]

[a]Department of Mechanical Engineering, Berkeley Sensor & Actuator Center, University of California, Berkeley, CA 94720, USA

[b]Department of Mechatronics Engineering, Kangwon National University, 1 Kangwon-daehak-gil, Chuncheon 200-701, Republic of Korea

[*]**Corresponding Author: E-mail** mems@kangwon.ac.kr

Abstract

This paper presents a microfluidic pump operated by an asymmetrically deformed membrane, which was inspired by caterpillar locomotion. Almost all mechanical micropumps consist of two major components of fluid halting and fluid pushing parts, whereas the proposed caterpillar locomotion–inspired micropump has only a single, bilaterally symmetric membrane-like teardrop shape. A teardrop-shaped elastomeric membrane was asymmetrically deformed and then consecutively touched to the bottom of the chamber in response to pneumatic pressure, thus achieving fluid pushing. Consecutive touchdown motions of the teardrop-shaped membrane mimicked the propagation of a caterpillar's hump during its locomotory gait. The initial touchdown motion of the teardrop-shaped membrane at the centroid worked as a valve that blocked the inlet channel, and then, consecutive touchdown motions pushed fluid in the chamber toward the tail of the chamber connected to the outlet channel. The propagation of touchdown motion of the teardrop-shaped membrane was investigated using computational analysis as well as experimental studies. This caterpillar locomotion–inspired micropump composed of only a single membrane can provide new opportunities for simple integration of microfluidic systems.

Lab on a Chip Accepted Manuscript

Introduction

Microfluidics play a key role in medical, biological, and precise chemical applications[1]. Micropumps for precise liquid transportation[2-4], microvalves for halting or controlling the flow of a fluid[5], micromixers for uniform and fast mixing of two or more agents[6, 7], and microheaters for localized temperature control[8, 9] are essential components in microfluidic systems. Among these microfluidic components, the configuration of micropumps is more complex than that of other microfluidic components[2-8]. Multifunctional microfluidic systems such as the micro total analysis system (micro-TAS) require a micropump for the transportation of liquid samples at the right place and the right time[10]. Therefore, active micropumps are more appropriate than capillary-based, passive micropumps such as microchannel types[11-14] and paper types[15-17] for multifunctional microfluidic systems. However, precise micropumps are typically fabricated by silicon micromachining technologies[2-4]. After the polydimethylsiloxane (PDMS) casting process has been developed[18], many microfluidic devices were made with PDMS because of easy fabrication, biocompatibility, and low cost[19]. Therefore, for full integration with micropumps and microfluidic components of microchannels and micromixers, PDMS micropumps are more suitable than silicon-based micropumps.

Depending on pumping pressure generation methods, mechanical micropumps can be classified into three categories, including gas generation types (**Fig.1A**), electrokinetic flow types (**Fig.1B**), single membrane actuation with two valves types (**Fig.1C**), and peristaltic three membrane actuation types (**Fig.1D**), as shown in **Fig.1**. In the gas generation type, oxygen gas from hydrogen peroxide[20] and electrolytic bubbles from water[21] were used. Micropumps based on gas generation, however, require microheaters for the chemical reaction. Although electrokinetic, electroosmotic, pumping methods[22] required no any other mechanical components

Lab on a Chip Accepted Manuscript

except microchannels, only electrolyte could be transported. In the case of single membrane actuation with two valves, downward actuation of a membrane pushes liquid in the chamber, and two valves determine the pumping direction. In these types, liquid would just oscillate, and not transport without valves. The membrane can be actuated using piezoelectric, pneumatic, thermo-pneumatic, electrostatic, and electromagnetic methods. Valves can be generally classified into mechanical check valves such as flap[23], membrane[24], and ball structures[25] and hydrodynamic valves[5] such as nozzle/diffuser[26], Tesla structure[27], and asymmetric obstacle variations[28]. Hydrodynamic valves are sometimes referred to as "valveless"; however, nozzles/diffusers, Tesla structures, and asymmetric obstacles are obviously valves without moving parts from the viewpoint of structure. For a peristaltic micropump with three membranes, the center membrane pushes liquid, and the left and right membranes work as valves, as shown in **Fig. 1D**[29]. Because the configuration of the three membranes is similar, the fabrication process of peristaltic micropumps is simple compared to that of micropumps based on a single membrane with two valves[30, 31]. The three membranes in the peristaltic pump can also be actuated through piezoelectric[29], electrostatic[30], thermo-pneumatic[31], pneumatic[32], and electromagnetic[33] methods. Besides the four previously described pumping methods, special techniques such as bacteria motion[34], acoustic actuation[35], and hydrogel expansion[36] were investigated for liquid pumping.

Previously reported mechanical micropumps have several disadvantages regarding integration with microfluidic systems. Gas generation–type micropumps inevitably require an additional microheater for chemical reactions and need special strategies for on/off control of the microheater. For the micropump based on a single membrane with two valves, the fabrication process is complicated because of the configurations and materials of the membrane and valves. Although the fabrication process of a peristaltic micropump using three membranes is relatively

Lab on a Chip Accepted Manuscript

simpler than that of the other two types; three different but synchronized operating signals are required for the precise actuation of membranes.

Since microfluidic platforms for biological, biomedical, chemical applications are generally made of PDMS, the integration of electrical components such as electrodes and piezoelectric discs cause the system complexity and expensive costs. Therefore, for full integration with micropumps and microfluidic components of microchannels and micromixers, micropumps made of a single material with fewer components are required. In this paper, a simple micropump operated using only a single membrane without additional valves and membranes is investigated. The operational principle of the suggested micropump was inspired by *Pleurotya* caterpillar locomotory gaits[37] similar to the propagation of waves. As shown in **Fig.2A**, a gait step is determined by anchoring the end of a caterpillar's body. A wave of contraction, followed by relaxation runs along the body from tail to head, producing the characteristic travelling hump along a caterpillar's back[37]. If the touchdown motion of an elastomeric membrane is propagated from the inlet to the outlet channel, like the motion propagation of a caterpillar's hump (**Fig.2B**), the fluid in the chamber can be transported from left (inlet) to right (outlet) without any additional components. In order to realize this **C**aterpillar **L**ocomotion–**i**nspired **M**icro**P**ump (CLiMP), bilaterally symmetric membranes (teardrop shape) were considered, as seen in the image showing the top view of the membrane at the top left in **Fig.3**.

Theoretical Model and Computational Estimation

To design a simple teardrop-shaped membrane, two circles with radii of 2 mm and 0.5 mm, were connected by tangent lines. The two circles were spaced as much as 5 mm apart, from center to center. The shape of the chamber underneath the teardrop-shaped membrane was also

Lab on a Chip Accepted Manuscript

the same as that of the membrane. The thickness of the membrane and the height of the chamber were 20 μm and 200 μm, respectively. For the theoretical estimation of the teardrop-shaped membrane, the simplified model based on the consecutive circular membranes with different radius was suggested as shown in **Fig.S1A**. Typical analytic relationship between the static pressure and deflection for a circular membrane with the radius (r), thickness (t), elastic modulus (E), and Poisson's ratio (ν) is given by

$$P = \left(\frac{Et^4}{r^4}\right)\left[k_1\left(\frac{\delta_{max}}{t}\right) + k_2\left(\frac{\delta_{max}}{t}\right)^3\right] \quad (1)$$

where P is the applied pneumatic pressure and δ_{max} is the maximum deflection of the membrane.[38] For the membrane with a fixed edge, k_1 = 5.33/(1-ν) and k_2 = 2.6/(1-ν^2).[38] In the estimation of the membrane deflection, elastic modulus (E) and thickness of the membrane (t) was considered as 1.8 MPa[39] and 20 μm, respectively. **Figure S1B** shows the membrane deflection, which was calculated using Eq.(1), of each circular shape at the center in response to the different applying pneumatic pressure. For the same pneumatic pressure, the center deflection of the circular membrane was decreased as the radius decreased. As a result, the touchdown motion of the consecutive circular membrane was propagated from the large circular membrane to the small circular membrane. Through this simplified model based on the combination of the consecutive circular membranes, the sequent propagation of touchdown motion from the large circular membrane to the small one could be verified in the teardrop-shaped membrane.

In order to verify the contact behavior between the PDMS membrane and the bottom of the chamber, the transient analysis was performed using the finite element analysis tool ANSYS. For the first computational work, an elastic model was considered because the maximum strain was

Lab on a Chip Accepted Manuscript

less than 8% along the edge of the teardrop-shaped membrane during the preliminary steady state simulation. For the better estimation, the viscoelastic approach such as the Mooney-Rivlin model, which is more appropriate when the PDMS membrane has relatively fast dynamic deformation, will need to be considered.[38] **Figure 3** shows the results of the computational analysis for the sequential contraction motion of the PDMS membrane at a pneumatic pressure of 5 kPa for 80 ms. The geometric centroid of the teardrop-shaped membrane was first moved and then touched down to the bottom of the chamber within 3 ms. After the centroid of the membrane touched down, the contact between the membrane and the bottom moved toward the tail of the teardrop-shaped chamber, similar to caterpillar locomotion. Transitional touchdown motions, contraction motions, of the PDMS membrane were completed within 80 ms. After 80 ms, the deformation of the membrane was not significantly changed. In other words, the membrane was quickly moved down during the initial 3 ms and then, the contact region was slowly propagated toward the tail of the teardrop-shaped chamber. During contraction motion of the PDMS membrane, the fluid in the chamber was pushed and transported from the inlet (head of the teardrop-shaped chamber) to the outlet (tail of the teardrop-shaped chamber). In addition, the hydraulic resistance in the chamber was also increased from the head to the tail of the teardrop-shaped chamber as shown in **Fig.4**. **Figure 4** shows the ratio of the hydraulic resistance at six different positions in the teardrop-shaped chamber for each time step. Hydraulic resistances were normalized by that of each position #3, where the centroid of the teardrop-shaped chamber passes across. As the touchdown motion of the membrane propagates, the peak of hydraulic resistance in each time step also propagates from left (head) to right (tail). The overall hydraulic resistances were increased as the contraction motion progressed because of reduced cross sectional area for flow path as indicated in **Fig.4**. Therefore, the main transport mechanism of the CLiMP for pumping

Lab on a Chip Accepted Manuscript

is the propagation of the touchdown motion of the PDMS membrane over the teardrop-shaped chamber and corresponding propagation of the hydraulic resistance from the inlet toward the outlet.

When pneumatic pressure was removed, the PDMS membrane was physically relaxed to the original shape before the contraction motion. In the relaxation process, fluid would refill the chamber through the inlet microchannel connected to the head of the teardrop-shaped chamber due to the different pressure loss between the inlet and outlet regions. In general, the irreversible pressure drop depends on the diffuser angle and the Reynolds number, *Re*[40]. The tendency of pressure losses with respect to the diffuser angle highly depends on *Re* because of non-negligible shear stresses[40]. At high Reynolds numbers (*Re* > 200), the pressure loss increases as the diffuser angle increases [41]. On the other hand, at low Reynolds numbers (*Re* < 10), the pressure loss decreases significantly as the diffuser angle was increases[40]. In the teardrop-shaped chamber, the diffuser angle formed by the head connected to the inlet channel, θ_{in}, was larger than that formed by the tail connected to the outlet channel, θ_{out}, as shown in the inset of **Fig.3**. The diffuser angles of θ_{in} and θ_{out} at 0.1 mm apart from the inlet and outlet microchannels were 143.6° and 47.1°, respectively. Referring to Rosa and Pinho's work[40], the pressure loss at the outlet region (θ_{out} = 47.1°) was approximately 2.14 times higher than one at the inlet region (θ_{in} = 143.6°) for the Reynolds number of 5. Therefore, a greater volume of inward flow into the chamber would be generated from the inlet channel, rather than from the outlet channel, during the relaxation process of the PDMS membrane.

Lab on a Chip Accepted Manuscript

Materials and Methods

Fabrication

The CLiMP consisted of three PDMS layers, including a teardrop-shaped chamber for fluid, a membrane for generating caterpillar-like motion, and an upper chamber for applying pneumatic pressure. Molds of the teardrop-shaped and upper chambers were made of SU-8 photoresist (MicroChem, Newton, MA), and the PDMS membrane was prepared using a spin coating process. Each layer of the CLiMP was fabricated using a PDMS (Sylgard 184, Dow Corning, NY) casting process, and then three layers were bonded together by an oxygen plasma treatment, as shown in **Fig. S2**. **Figures S3A** and **S3B** show SEM image of the cross section of the fabricated CLiMP and enlarged view of the PDMS membrane, respectively. The upper circular chamber for applying pneumatic pressure was not shown in **Figs.S3A** and **S3B.**

Experimental Setup

The experimental setup is shown in **Fig.S3C**. **Figure S3E** shows schematic view of the membrane deformation when the pneumatic pressure is applied. The pneumatic pressure supplied by the hydrogen gas tank was monitored using a pressure sensor and controlled by a small-sized solenoid valve. The on/off signal for the solenoid valve was controlled via the combination of a function generator and voltage amplifier. The motion of the teardrop-shaped, bilaterally symmetric PDMS membrane was captured using a high-speed camera, which sampled every 790 μs. The flow rate was determined by measuring the length of the traveled fluid through a 580 μm diameter tube in 5 min. The pneumatic pressure applied to the membrane, solenoid valve control signals, motion of the membrane, and flow through the tube were recorded simultaneously.

Lab on a Chip Accepted Manuscript

Results and Discussion

High-Speed Motion Capture and Analysis

For the experimental study, the teardrop-shaped chamber connected with inlet and outlet microchannels of 200 μm in width was fabricated. It was necessary to experimentally confirm the propagation of the membrane touchdown motion estimated through computational analysis, as shown in **Figs.3** and **4**. Thus, sequential motions of the membrane were captured using a high-speed camera; these results were compared with computational simulation results. **Figure 5** shows the sequential images of the teardrop-shaped membrane operated at a duty cycle of 20% and a pneumatic pressure of 5 kPa at 2 Hz, as indicated in the graph at the bottom right in **Fig. 5**. Images were selected every 20 ms in the contraction process, and selected every 40 ms in the relaxation process of the membrane. The dark regions represent the fluid (1% methylene blue) filled in the teardrop-shaped chamber; the upper pneumatic chamber was invisible because the lens focused on the membrane.

Using the images captured by a high-speed camera, experimental results were compared with simulation results in the aspect of the touchdown (contact) area between the PDMS membrane and the bottom of the teardrop-shaped chamber. **Figure S4** presents the comparison of the contact area during the contraction period. The contact area was increased during the contraction period in both simulation and experimental results. However, the discrepancy between the estimated and experimental results was increased as the contract area was increased. Again, this implies that the viscoelastic model could be better than the elastic model for the large and fast dynamic deformation.

The 20 μm thick PDMS membrane had an initial deformation drawing down into the chamber caused by the surface tension of the fluid in the chamber. Thus, the centroid region of

Lab on a Chip Accepted Manuscript

the teardrop-shaped chamber was slightly bright. After applying pneumatic pressure, the membrane quickly moved downward and entirely contacted with the bottom of the chamber at approximately 100 ms. This means that the pneumatic pressure must be applied for at least 100 ms to complete the touchdown motion. If not (i.e. pressure was applied for less than 100 ms), the touchdown motion of the membrane stops in the middle of the propagation and restores to the initial state. It was found that the same situation occurred when the amplitude of pneumatic pressure was lower than 5 kPa. When pneumatic pressure was applied to the membrane, there was a rising time (i.e. time lag) of about 40 ms, as shown in **Fig. 5**. As a result, the membrane largely deformed after 40 ms. The total elapsed time for the contraction process through the experiments was 100 ms, which is similar to one estimated via computational analysis (80 ms). Then, the membrane was restored to its initial position about 200 ms after removing the pneumatic pressure. For the restoration of the membrane to initial position, twice the amount of time was needed than for contraction process. Based on the analysis of high-speed motion capture, the contraction period (CP) of 100 ms and relaxation period (RP) of 200 ms were required for the one cycle of the contraction and relaxation processes. (**Movie S1**). For the proper operation of the CLiMP, a parametric study to find an appropriate combination of the CP and RP was performed.

Flow Rate Measurement

To investigate the pumping capacity of the CLiMP, the amplitude, frequency, and duty cycle of the applied pneumatic pressure to the teardrop-shaped PDMS membrane were controlled as 3–5 kPa with a 1 kPa step, 0.5–5 Hz with a 0.5 Hz step, and 20–80% with a 15% step, respectively. **Movie S2A**, **S2B**, and **S2C** presents the example of the flow rate generated by the CLiMP at

Lab on a Chip Accepted Manuscript

different operational condition. **Figures 6A, 6B,** and **6C** show the measured flow rates generated by the CLiMP with three different pneumatic pressures of 3, 4, and 5 kPa, respectively. For a pressure less than 2 kPa and greater than 6 kPa, the CLiMP generated no flow rate, because the propagation of the touchdown motions could not occur. At pneumatic pressures of 3–5 kPa, the overall flow rate increased as the pneumatic pressure increased. For low pneumatic pressures less than 5 kPa (i.e. **Figs.6A** and **6B**), the propagation of the touchdown motion of the PDMS membrane was limited to the area near the centroid of the teardrop-shaped chamber resulting in decreased flow rate. When the CLiMP was operated at a 20% duty cycle, 1.5 Hz frequency (CP/RP = 133 ms/533 ms) and 5 kPa pneumatic pressure, the maximum flow rate (18.3 μL/min) was observed. For the flow rate at a pneumatic pressure of 5 kPa (**Fig.6C**), the combination of duty cycle and frequency was converted into the combination of the CP and RP, showing the flow rates with respect to the CP and RP as shown in a contour graph in **Fig.6D**. The maximum and minimum flow rates were observed at a different RP while the CP for both rates has a similar value of approximately 150 ms. This result indicates that the flow rate depended considerably on the RP rather than CP. For the fixed CP of 133 ms (along the y-axis in **Fig.6D**), the flow rate rapidly increased as the RP increased. On the other hand, for the fixed RP of 533 ms (along the x-axis in **Fig.6D**), the flow rate was gradually changed with a gentle slope as the CP increased. Moreover, there were certain conditions that resulted in no flow rate generation, as shown in **Fig.6D**. When the RP was less than 80 ms, no flow rate was generated (Region II in **Fig.6D**). On the other hand, the CLiMP was properly operated, even though the contraction period was only 40 ms (Region I in **Fig. 6D**). Therefore, the RP at which fluid was refilled in the chamber is an important factor for the operation of the CLiMP.

Lab on a Chip Accepted Manuscript

Figure S5 shows the measured flow rate with the different duty cycles (20, 50 and 80%) for each different pneumatic pressure (3, 4 and 5 kPa) in response to the frequencies (1–5 Hz). The number of pushing membrane per second was determined by the frequency of the pneumatic pressure, and the both propagation time of touchdown motion (contraction period, CP) and liquid refilling time (relaxation period, RP) were determined by the duty cycle. For example, for the frequency and duty cycle of 2 Hz and 20%, the number of pushing process, CP, and RP were twice a second, 0.4 sec., and 1.6 sec, respectively. Regardless of duty cycles, the flow rate generated by the CLiMP was increased as pneumatic pressure increased. However, the peak of the measured flow rate was observed at a different frequency of the applied pneumatic pressure. At a duty cycle of 20 and 50%, the maximum flow rates were measured at 1.5 and 2.5 Hz, respectively. Through the experiments, it was found that the flow rate traded off the number of pushing process, the CP and RP. As a result, at 20% duty cycle (**Fig.S5A**), the CP was too short to propagate the touchdown motion at a frequency higher than 2 Hz, thus the maximum flow rate was measured at 1.5 Hz. On the other hand, at 50% duty cycle (**Fig.S5B**), the RP was relatively shorter than the CP to refill the liquid above 3 Hz, thus the maximum flow rate was generated at 2.5 Hz. It was also found that at 50% duty cycle, the flow rate was linearly proportional to the frequency up to 2.5 Hz where the peak value occurs, resulting in easy control of the flow rate by the combination of the frequency and amplitude of pneumatic pressure. Finally, at 80% duty cycle (**Fig.S5C**), the pumping operation was significantly limited by the RP as no flow rate was generated at the frequency higher than 2.5 Hz due to insufficient liquid refilling.

The hydraulic head was measured during the operation at 20% duty cycle, 1 Hz frequency and 5 kPa pneumatic pressure. **Figures 7A** and **7B** show the sequential images of the hydraulic head and the estimations of the hydraulic head with respect to operation time based on the height

Lab on a Chip Accepted Manuscript

difference between vertical inlet and outlet tube (see **Movie S3**). The hydraulic head generated by the CLiMP was linearly increased up to 350 Pa and then saturated at 373 ± 19 Pa, indicating that the pumping pressure of the CLiMP was approximately 370 Pa. In general, microfluidic pumps with check valves provided a higher hydraulic head than valveless-type micropumps[2]. The low pumping pressure of the CLiMP results from the relatively low operating pneumatic pressure of 5 kPa and the inert fluids in the dead volume between the vertical wall of the teardrop-shaped chamber and the membrane during the contraction period. Therefore, if the CLiMP is operated at a high pneumatic pressure by reducing the size of the teardrop-shaped chamber, the pumping pressure is expected to increase as well as reduced relaxation period due to the increased membrane stiffness. The teardrop-shaped chamber with a rounded wall providing tight sealing during the touchdown motion of the asymmetric membrane is also expected to have a higher pumping pressure than one having a vertical wall.

Conclusion

This paper reports on the valveless microfluidic pump inspired by caterpillar locomotion. The proposed CLiMP consists of a single asymmetric membrane without any additional components. Using the bilaterally symmetric teardrop-shaped membrane and chamber, the consecutive propagation of the touchdown motion was realized and verified by both computational and experimental results. The fabricated CLiMP requires a relaxation period at least twice longer than the contraction period since the flow rate strongly depends on the relaxation period, rather than the contraction period. The maximum flow rate (18.3 μL/min) was achieved by the combination of a contraction period of 133 ms and a relaxation period of 533

Lab on a Chip Accepted Manuscript

ms. The CLiMP will provide new opportunities for the integration of micropumps to the various microfluidic applications due to its simplicity.

Acknowledgements

This work was supported by the Pioneer Research Center Program through the National Research Foundation of Korea funded by the Ministry of Science, ICT & Future Planning (2012-0009575), and was also supported by the Human Resources Development program (No.20134030200240) of the Korea Institute of Energy Technology Evaluation and Planning (KETEP) grant funded by the Korea government Ministry of Trade, Industry and Energy. This work was also partially supported by the KAUST Global Collaborative Research (GCR) under Academic Excellence Alliance and Partnership Program.

Lab on a Chip Accepted Manuscript

References

1. G. M. Whitesides, *Nature*, 2006, **442**, 368-373.
2. N.-T. Nguyen, X. Huang and T. K. Chuan, *J. Fluids Eng.*, 2002, **124**, 384-392.
3. D. Laser and J. Santiago, *J. Micromech. Microeng.*, 2004, **14**, R35.
4. B. D. Iverson and S. V. Garimella, *Microfluid. Nanofluid.*, 2008, **5**, 145-174.
5. K. W. Oh and C. H. Ahn, *J. Micromech. Microeng.*, 2006, **16**, R13.
6. V. Hessel, H. Löwe and F. Schönfeld, *Chem. Eng. Sci.*, 2005, **60**, 2479-2501.
7. N.-T. Nguyen and Z. Wu, *J. Micromech. Microeng.*, 2005, **15**, R1.
8. C. Y. Jin, Z. Li, R. S. Williams, K.-C. Lee and I. Park, *Nano Lett.*, 2011, **11**, 4818-4825.
9. J. Wu, W. Cao, W. Wen, D. C. Chang and P. Sheng, *Biomicrofluidics*, 2009, **3**, 012005.
10. M. A. Burns, B. N. Johnson, S. N. Brahmasandra, K. Handique, J. R. Webster, M. Krishnan, T. S. Sammarco, P. M. Man, D. Jones and D. Heldsinger, *Science*, 1998, **282**, 484-487.
11. M. Zimmermann, H. Schmid, P. Hunziker and E. Delamarche, *Lab Chip*, 2007, **7**, 119-125.
12. N. S. Lynn and D. S. Dandy, *Lab Chip*, 2009, **9**, 3422-3429.
13. K. K. Lee and C. H. Ahn, *Lab Chip*, 2013.
14. P. Novo, F. Volpetti, V. Chu and J. P. Conde, *Lab Chip*, 2013, **13**, 641-645.
15. A. W. Martinez, S. T. Phillips and G. M. Whitesides, *Proc. Natl. Acad. Sci.*, 2008, **105**, 19606-19611.
16. A. W. Martinez, S. T. Phillips, G. M. Whitesides and E. Carrilho, *Anal. Chem.*, 2010, **82**, 3-10.
17. B. R. Lutz, P. Trinh, C. Ball, E. Fu and P. Yager, *Lab Chip*, 2011, **11**, 4274-4278.
18. D. C. Duffy, J. C. McDonald, O. J. Schueller and G. M. Whitesides, *Anal. Chem.*, 1998, **70**, 4974-4984.
19. J. C. McDonald and G. M. Whitesides, *Acc. Chem. Res.*, 2002, **35**, 491-499.
20. Y. H. Choi, S. U. Son and S. S. Lee, *Sens. Actuators, A*, 2004, **111**, 8-13.
21. S.-H. Chiu and C.-H. Liu, *Lab Chip*, 2009, **9**, 1524-1533.
22. C. Rice and R. Whitehead, *J. Phys. Chem.*, 1965, **69**, 4017-4024.
23. H. Van Lintel, F. Van de Pol and S. Bouwstra, *Sens. Actuators*, 1988, **15**, 153-167.
24. D. Bien, S. Mitchell and H. Gamble, *J. Micromech. Microeng.*, 2003, **13**, 557.
25. M. Carrozza, N. Croce, B. Magnani and P. Dario, *J. Micromech. Microeng.*, 1995, **5**, 177.
26. E. Stemme and G. Stemme, *Sens. Actuators, A*, 1993, **39**, 159-167.
27. N. Tesla, U.S. Patents No.1,329,559, 1920.
28. H. Sheen, C. Hsu, T. Wu, C. Chang, H. Chu, C. Yang and U. Lei, *Microfluid. Nanofluid.*, 2008, **4**, 331-342.
29. J. G. Smits, *Sens. Actuators, A*, 1990, **21**, 203-206.
30. J. Xie, J. Shih, Q. Lin, B. Yang and Y.-C. Tai, *Lab Chip*, 2004, **4**, 495-501.
31. O. C. Jeong, S. W. Park, S. S. Yang and J. J. Pak, *Sens. Actuators, A*, 2005, **123**, 453-458.
32. H. Lai and A. Folch, *Lab Chip*, 2011, **11**, 336-342.
33. C. Yamahata, C. Lotto, E. Al-Assaf and M. Gijs, *Microfluid. Nanofluid.*, 2005, **1**, 197-207.
34. M. J. Kim and K. S. Breuer, *Small*, 2008, **4**, 111-118.
35. S. Wang, X. Huang and C. Yang, *Microfluid. Nanofluid.*, 2010, **8**, 549-555.
36. A. Richter, S. Klatt, G. Paschew and C. Klenke, *Lab Chip*, 2009, **9**, 613-618.

Lab on a Chip Accepted Manuscript

37. J. Brackenbury, *Nature*, 1997, **390**, 453-453.
38. S.-H. Yoon, V. Reyes-Ortiz, K.-H. Kim, Y. H. Seo and M. R. Mofrad, *Microelectromechanical Systems, Journal of*, 2010, **19**, 854-864.
39. K. Khanafer, A. Duprey, M. Schlicht and R. Berguer, *Biomed. Microdevices*, 2009, **11**, 503-508.
40. S. Rosa and F. Pinho, *Int. J. Heat Fluid Flow*, 2006, **27**, 319-328.
41. V. Singhal, S. V. Garimella and J. Y. Murthy, *Sens. Actuators, A*, 2004, **113**, 226-235.

Lab on a Chip Accepted Manuscript

Figure Legends

Fig. 1 Configuration comparison of various micropumps, depending on pumping pressure generation methods: (A) Gas generation, (B) Electrokinetic or electroosmotic pumping, (C) Single membrane actuation with two valves, (D) Peristaltic three membrane actuation.

Fig. 2 Comparison of caterpillar locomotion and mimetic micropump: (A) Main locomotory gaits in Pleurotya caterpillar, (B) Membrane motions of caterpillar locomotion-inspired micropump.

Fig. 3 Computational analysis showing transient response of a bilateral symmetric teardrop-shaped membrane motion: touchdown motion propagated from left to right, similar to caterpillar locomotion.

Fig. 4 Transitional change in hydraulic resistance in teardrop-shaped chamber, based on computational analysis with each time step. The hydraulic resistance also consecutively increased from left to right during the propagation of touchdown motion.

Fig. 5 Sequential images of asymmetric PDMS membrane motion captured by a high-speed camera at a 20% duty cycle, 2 Hz frequency and 5 kPa pneumatic pressure: contraction process was completed within 100 ms while 200 ms was required for the relaxation process. Scale bar indicates 1 mm.

Fig. 6 Measured flow rate with respect to the duty cycle and frequency under different amplitude of applied pneumatic pressure: (A) Pneumatic pressure of 3 kPa, (B) 4 kPa, (C) 5 kPa, (D) 2D contour graph with contraction and relaxation periods at 5 kPa.

Fig. 7 Hydraulic head generated by the caterpillar locomotion–inspired micropump at a 20% duty cycle, 1 Hz frequency and 5 kPa pneumatic pressure: (A) Sequential images of the pumping fluid every 10 s, (B) Calculated hydraulic head based on the height difference between inlet and outlet tube.

Lab on a Chip Accepted Manuscript

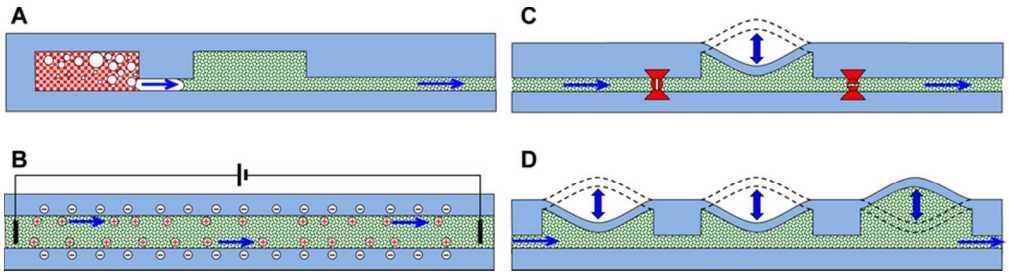

77x20mm (300 x 300 DPI)

Lab on a Chip Accepted Manuscript

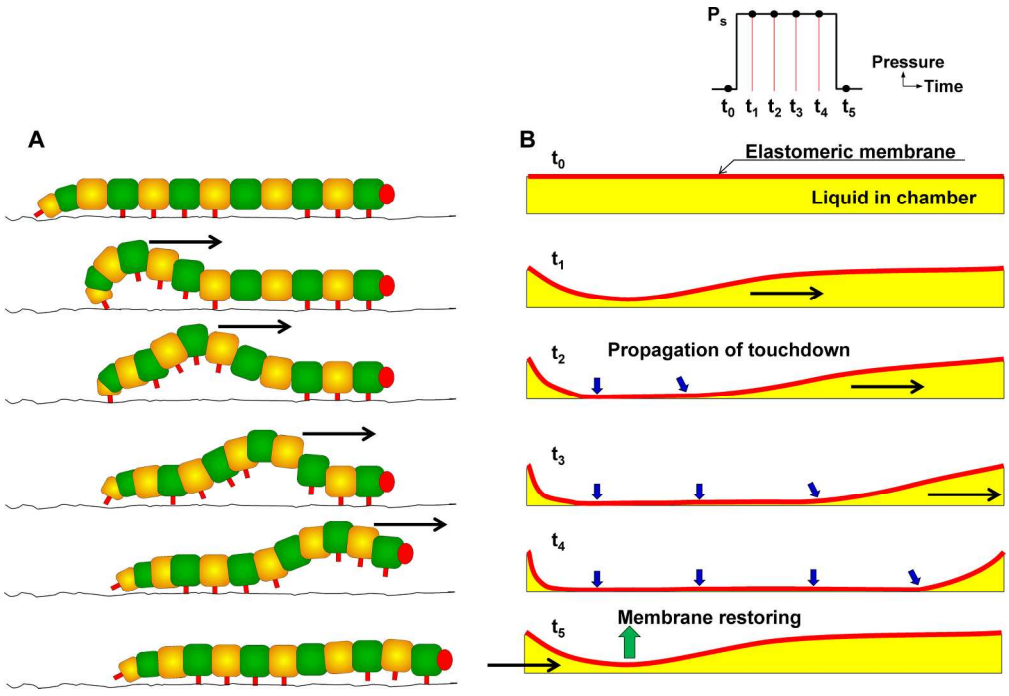

199x136mm (300 x 300 DPI)

Lab on a Chip Accepted Manuscript

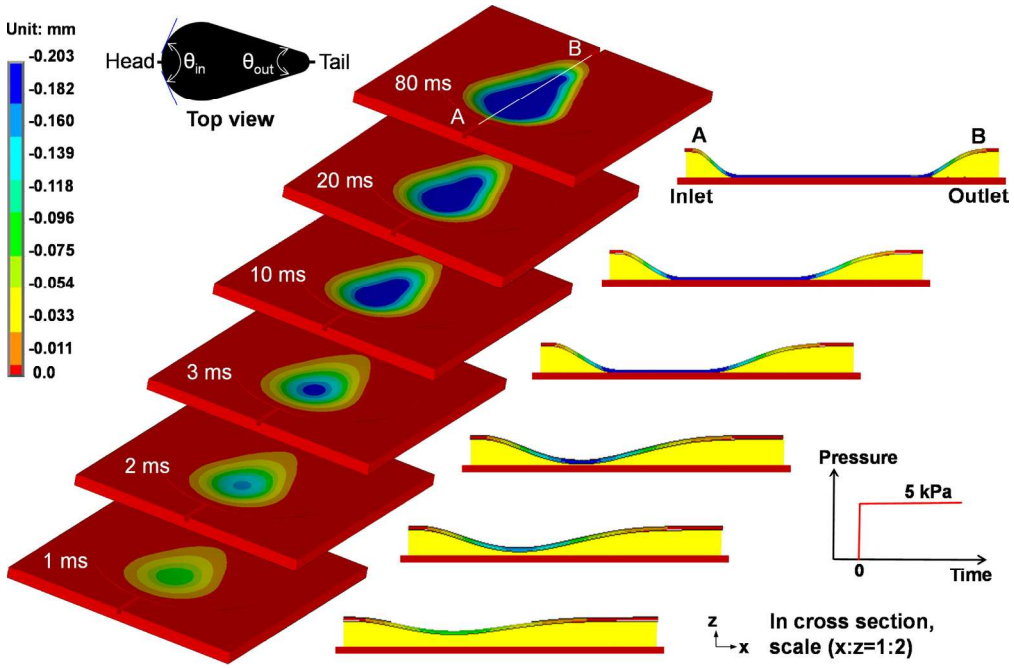

191x125mm (300 x 300 DPI)

Lab on a Chip Accepted Manuscript

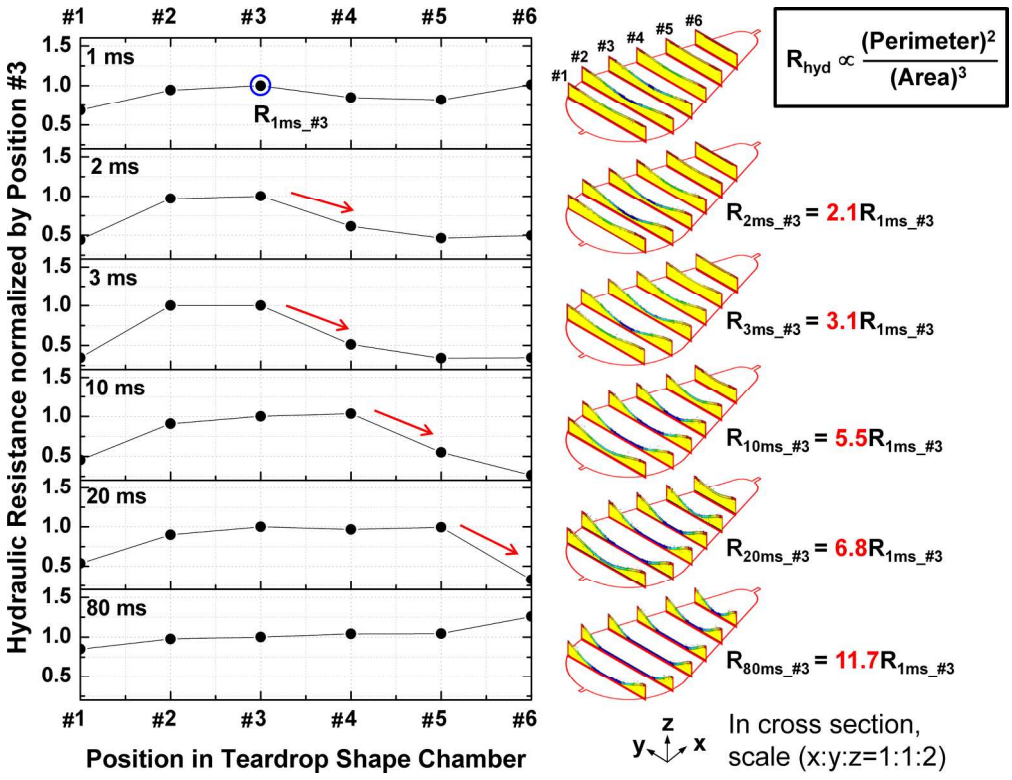

195x149mm (300 x 300 DPI)

Lab on a Chip Accepted Manuscript

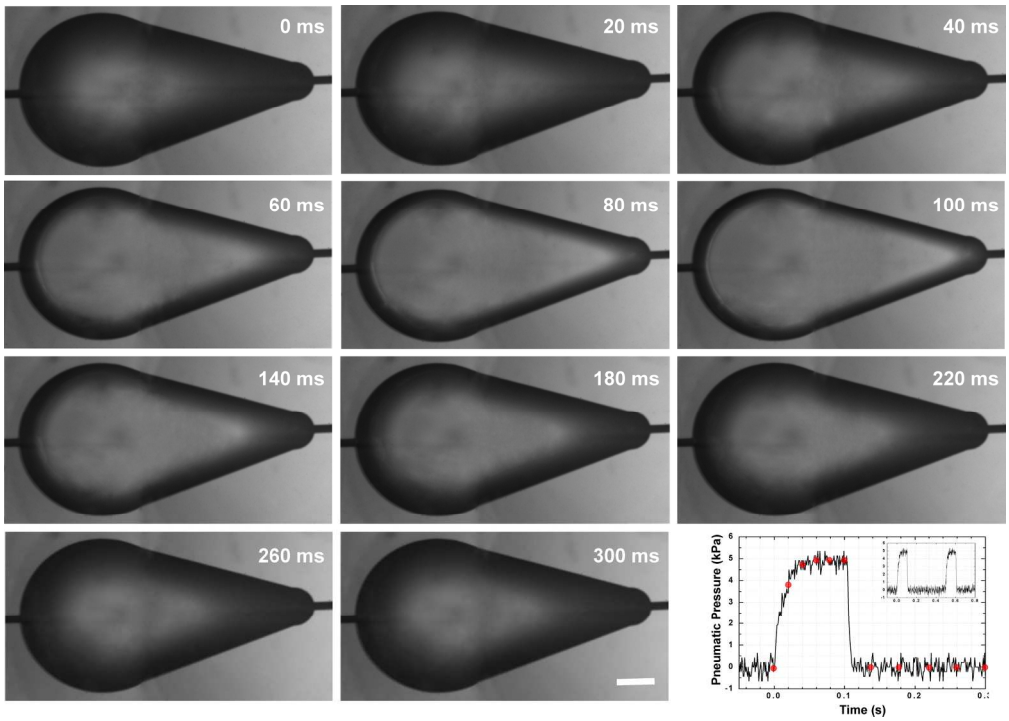

191x136mm (300 x 300 DPI)

Lab on a Chip Accepted Manuscript

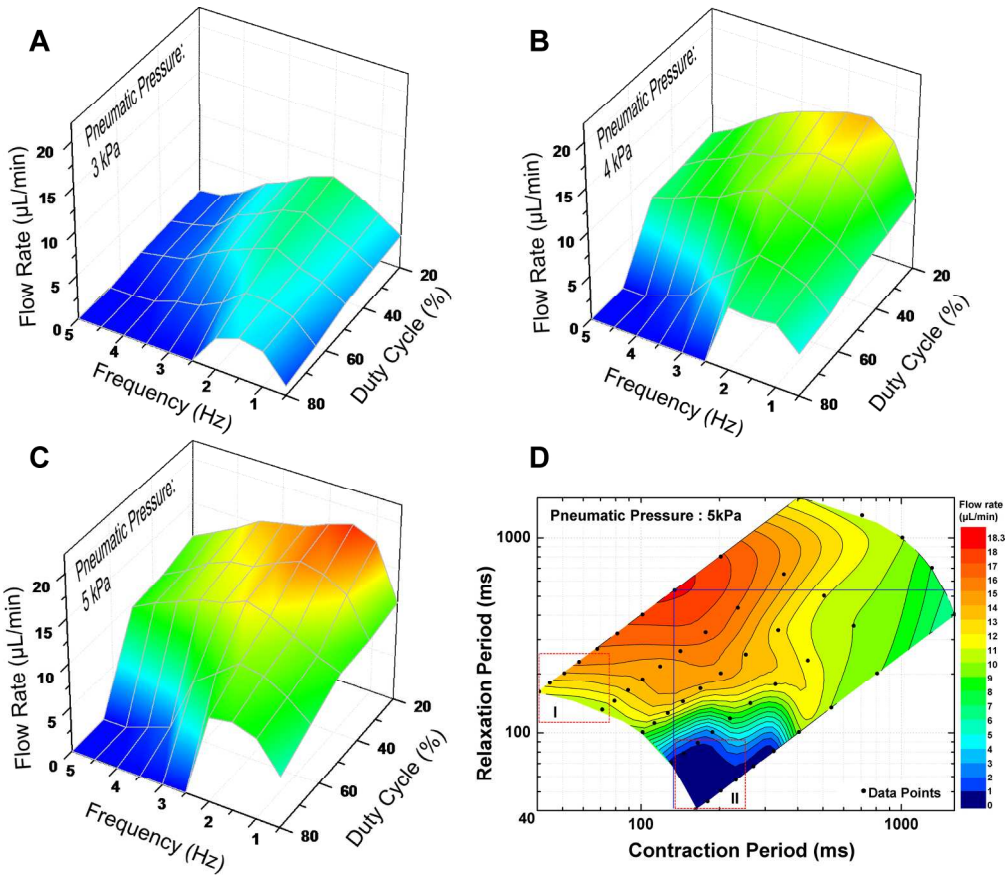

203x176mm (300 x 300 DPI)

Lab on a Chip Accepted Manuscript

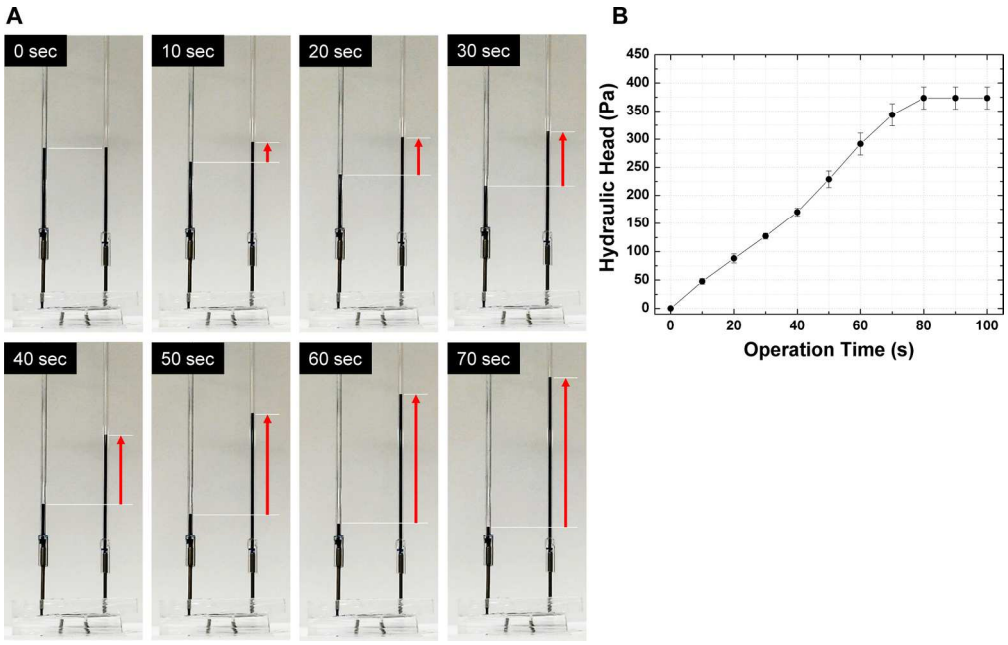

186x117mm (300 x 300 DPI)

Lab on a Chip Accepted Manuscript